Crystal structure and elastic and phonon properties of realgar versus pressure

Crystal structure, elastic and phonon properties of realgar versus pressure

Authors

Gianfranco Ulian[ab] and Giovanni Valdrè[ab]*

[a]Biological, Geological and Environmental Sciences, University of Bologna, P. Porta San Donato 1, Bologna, Emilia-Romagna, 40127, Italy

[b]Laboratory of Biomineralogy, Crystallography and Biomaterials, University of Bologna, P. Porta San Donato 1, Bologna, Emilia-Romagna, 40127, Italy

Correspondence email: giovanni.valdre@unibo.it

Synopsis The present work reports on a Density Functional Theory characterization of the crystal-chemical, elastic and phonon properties of realgar α-As_4S_4, a mineral made of cluster-like As_4S_4 molecules held together by weak van der Waals interactions that recently drew attention for possible optoelectronic applications. A challenge in dealing with theoretical methods with this kind of crystalline system is the inclusion of dispersive forces in the physical treatment and the correction of basis set superposition error in molecule-molecule interactions, which were both accounted for the first time in the present work using the PBEh-3c approach.

Abstract Realgar α-As_4S_4 (space group $P2_1/n$) is one of the best-known arsenic sulphide minerals because of its extended use in the past as red pigment and its employment in modern times for advanced optical and electronic technological applications. From a geological perspective, the main realgar deposits are hydrothermal and epithermal; nevertheless, it is also a relevant phase found between the upper mantle and Earth's crust and, therefore, one of the main sources of arsenic. Despite this widespread use and interest, few experimental and theoretical studies were focused on the characterisation of the structural, elastic, and vibrational properties of realgar, especially their variation with pressure. Some quantities, such as the cohesive energy between the As_4S_4 units and the elastic moduli have never been reported in the scientific literature. The present work deals with a Density Functional Theory investigation of the cited properties of realgar, using the recently proposed PBEh-3c method, in particular to deal with crystalline solids characterized by weak van der Waals interactions. This approach was validated against the available crystal-chemical, mechanical, and spectroscopic data from previous studies, finding a generally good agreement. The equation of state parameters of the energy *vs* unit cell volume data were V_0 = 767.13(9) Å^3, B_0 = 15.73(8) GPa and B' = 9.1(2), with the bulk modulus value (B_0) in good agreement with the value obtained from the elastic

tensor analysis (B = 16.1 GPa). The cohesive energy was found to be about 146.1 kJ mol^{-1}, a value that follows the typical ones of organic crystals. The present work provides new insights into this peculiar mineral that, from the mineralogical point of view, could be considered a prototype of a heterodesmic structure made by inorganic molecular clusters.

Keywords: Realgar As_4S_4, crystal structure, elastic and vibrational properties, pressure dependence, Density Functional Theory.

1. Introduction

The wide interest in arsenic chalcogenides dates back to ancient times when they were employed as mineral pigments in paintings, frescoes, decorations, hieroglyphs in papyri, and lacquers (Daniels & Leach, 2004, Li *et al.*, 2009, Ernst, 2010, Avlonitou, 2016, van Loon *et al.*, 2017). In recent years, these natural materials are drawing ever more continuous attention because they could be used in modern optical and electronic applications and devices (Bindi *et al.*, 2015).

Among the extensive series of As-S minerals, realgar α-As_4S_4 (space group $P2_1/n$, **Fig.1**) and orpiment As_2S_3 are the most abundant arsenic sulphides, as reviewed by Bonazzi and Bindi (2008). Both minerals are commonly found in veins and hot springs deposits, often associated with clays and limestones. Realgar contains As_4S_4 cages, the so-called "realgar-type" molecules, while orpiment is formed by bidimensional layers. Hence, both minerals are heterodesmic structures, *i.e.* solid crystals presenting different types of bonds. In the case of realgar, the molecular cages are formed by covalently bound As and S atoms, with two covalent As–S bonds and one metallic As–As bond per As atom. The As_4S_4 cluster units are held together by weak van der Waals interactions, creating a peculiar crystal with dispersive forces distributed in the three-dimensional space.

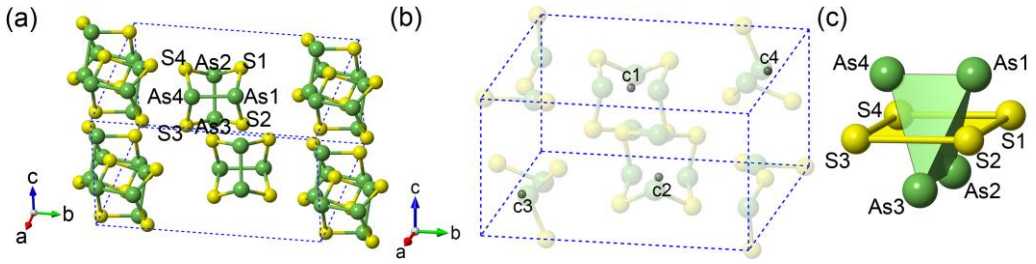

Figure 1 (a) Balls-and-sticks model of bulk α-As_4S_4 viewed from [111] direction. Panel (b) shows the positions of the centres of mass of the cage-like molecules. Panel (c) reports a geometrical representation of the As_4S_4 cage-like molecule, highlighting the As_4 disphenoic group and the S_4 planar square. Colour coding for atoms: green – As, yellow – S.

From a geological perspective, α-As_4S_4 is formed between the upper mantle and Earth's crust, where the pressure is in the range of 5–7 GPa and it also found in hydrothermal and epithermal deposits (e.g., see Yang *et al.*, 2021). For this means, the knowledge of the crystal structure and the elastic properties of this mineral is of utmost importance. In this context, experimental measurements of the α-As_4S_4 crystal structure versus pressure were carried out with energy-dispersive X-ray diffraction up to 6.52 GPa (Tuktabiev *et al.*, 2009) and by *in situ* single-crystal X-ray diffraction and powder diffraction up to 5.40 GPa (Hejny *et al.*, 2012). The elastic properties were described in both cases using the equation of state parameters resulting from the unit cell volume *vs* pressure data, but it is still not known the uniaxial and biaxial stress-strain response of the mineral, which is a piece of information typically reported in the second-order elastic moduli tensor. Furthermore, Zallen and Slade (1978) coupled the pressure state with the Raman spectrum of the mineral, an investigation performed also more recently by Hejny *et al.* (2012). However, no data were provided on the evolution of the infrared (IR) phonon frequencies with pressure.

Realgar is also a very interesting and challenging mineral phase in the context of Density Functional Theory (DFT) simulations. In the last decade, it was shown the extremely important role played by dispersive forces (London forces, hydrogen bonds, etc.) in determining the crystal-chemical, physical, elastic and thermodynamic properties in heterodesmic minerals (see for instance the works of Tunega *et al.*, 2012, Ulian & Valdrè, 2015, Ulian & Valdrè, 2018, 2019, Cutini *et al.*, 2020). Standard DFT functionals developed in the past usually underestimated the effect of these weak interactions, which is the reason behind the implementation of several correction schemes, starting from the pairwise –D2 and –D3 *a posteriori* corrections (Grimme, 2006, Grimme *et al.*, 2011) to the many-body dispersion model of Tkatchenko *et al.* (2012). To our knowledge, Hejny *et al.* (2012) proposed a combined experimental and theoretical investigation of the structural properties of realgar under hydrostatic compression. In their work, the authors performed DFT simulations using CRYSTAL06, a version of the code that did not include any correction schemes for the treatment of dispersive forces. More recently, Caratelli *et al.* (2017) simulated the structural, elastic, and vibrational properties of realgar with the DFT/PBE-D2 approach, which employs a generalized gradient approximation functional (PBE) and the DFT-D2 scheme. In the meanwhile, researchers developed correction methods for weak van der Waals interactions that are less empirical than the DFT-D2 approach, *i.e.*, these methods are generalized and do not introduce system-specific parameters. However, such corrections were not tested on realgar, which could be considered a prototype for minerals made of molecular clusters held together by 3D van der Waals interactions. Furthermore, it was never reported from either experimental measurements or theoretical simulations the strength of the interaction between the cage-like As_4S_4 molecules within the mineral. Finally, molecular-like minerals pose an additional issue in DFT simulations when using localized basis sets such as Gaussian-type orbitals (GTO) or

numerical atomic orbitals (NAO) because of the basis set superposition error (BSSE), which artificially increases the binding energy between the molecules.

For all these means, to fill these knowledge gaps, in the present study we report a complete investigation of the structural, elastic and vibrational properties of the α-As_4S_4 phase obtained by DFT simulations. The recently proposed PBEh-3c approach, which was developed mainly for organic crystalline solids and includes corrections for both long-range interactions and BSSE (*vide infra*), is used for the first time to describe of a cluster-like inorganic mineral, comparing the crystal structure at equilibrium and in compression with those available in the literature from both experimental and simulation works. After this approach, the elastic tensor of realgar is presented and discussed alongside with its derived quantities, e.g., the Young's modulus, considering both polycrystalline averages and single-crystal directional values. Last but not the less important, the evolution of both infrared and Raman normal modes v with pressure are thoroughly presented, using also the Grüneisen's formulation to describe the $v(V)$ behaviour.

2. Computational Methods

The CRYSTAL17 code (Dovesi *et al.*, 2018) was used for the *ab initio* simulations performed in the present work. Since realgar is made of cage-like As_4S_4 molecules held together by weak van der Waals interactions (see Fig.1), we employed the combined PBEh-3c method proposed by Grimme and collaborators (2015) to consider the dispersive forces contribution. The basis of this approach is represented by the total electronic energy, E_{tot}^{PBEh}, obtained from the global hybrid functional PBEh, which employs the well-known PBE generalized gradient approximation functional (Perdew *et al.*, 1996) and includes 42% of exact Hartree-Fock exchange. Then, two additional terms are calculated, the first one is the energy contribution arising from the long-range interactions, obtained from the DFT-D3 scheme described by Grimme *et al.* (2010), whereas the second one corrects the basis set superposition error (BSSE) using a geometrical counterpoise (gCP) approach, as explained by Kruse and Grimme (2012). The BSSE is an energy term introduced by the (necessarily) finite atomic basis sets, which artificially increases the strength of the interactions between atoms and molecules and needs to be removed. Thus, the total electronic energy of the system under consideration is semi-classically corrected, according to the following formula:

$$E_{tot}^{PBEh-3c} = E_{tot}^{PBEh} + E_{D3} + E_{BSSE}^{damped\ gCP} \quad (1)$$

with PBEh the density functional previously described, E_{D3} the energy term from the long-range interactions and $E_{BSSE}^{damped\ gCP}$ is the energy contribution from the geometrical counterpoise correction described by Grimme *et al.* (2015). This latter energy contribution was damped to avoid affecting the covalent bonding. As explained by Grimme *et al.* (2011), the damping is necessary to avoid both near-

singularities for small internuclear distances between pairs of atoms and double-counting effects of electron correlation at intermediate distances. In the present work, the van der Waals energy E_{D3} was calculated using the Becke-Johnson damping (Becke & Johnson, 2005) and the three-body dispersion of Axilrod-Teller-Muto, as suggested by Grimme *et al.* (2010). Further details of the formulations are not reported here for the sake of conciseness, and the interested reader can refer to the cited literature (see Grimme *et al.*, 2010, 2015).

The all-electron Gaussian type-orbitals basis set called def2-mSVP was adopted, which is a modified double-ζ orbital set (see Grimme *et al.*, 2015). The iterative self-consistent field (SCF) procedure to calculate the total energy is considered converged when the energy difference between two consecutive steps is lower than 10^{-8} Ha. The energy is calculated on a pruned grid of 75 points and 974 angular points, subdivided into 5 sub-intervals of 86, 194, 350, 974, and 350 points, which derives from the Gauss-Legendre quadrature and Lebedev schemes (see Prencipe *et al.*, 2004). The truncation criteria for the Coulomb and exchange integrals were 10^{-8}, and 10^{-18} for the pseudo-overlap parameter. In the periodic case, a 4 × 4 × 4 Monkhorst-Pack (1976) net with 30 *k* points in the reciprocal space was employed.

The crystal lattice and the atomic positions were optimized within the same run using the analytical gradient method for the atomic positions and a numerical gradient for the unit-cell parameters. The Hessian matrix is upgraded with the Broyden-Fletcher-Goldfarb-Shanno algorithm. For considering the geometry as converged, the tolerances for the maximum allowed gradient and the maximum atomic displacement have been set to 10^{-5} Ha bohr^{-1} and 4×10^{-5} bohr, respectively.

Harmonic frequencies were calculated in the Γ point (**q** = 0) by diagonalising the mass-weighted Hessian matrix *W* (dynamical matrix), whose elements are the second derivatives of the lattice potential with respect to mass-weighted atomic displacements (see Pascale *et al.*, 2004a):

$$W_{\alpha i,\beta j}(\Gamma) = \frac{H_{\alpha i,\beta j}}{\sqrt{M_\alpha M_\beta}} \quad (2),$$

with $H_{\alpha i,\beta j}$ the energy second derivative, M_α and M_β the atomic masses and the subscripts in latin (i, j) and in Greek letters (α, β) the atomic coordinates and the atoms, respectively. The calculated frequencies were scaled by 0.95 because of the use of the combined PBEh-3c approach, as suggested by Grimme and collaborators (2015).

The elastic moduli are the components of the 4th-rank stiffness tensor **C** that, according to Voigt's 6×6 matrix representation (Nye, 1957), can be written as

$$\sigma_v = C_{vu}\eta_u \quad (3)$$

where the indices *v*,*u* run from 1 to 6 (1 = *xx*, 2 = *yy*, 3 = *zz*, 4 = *yz*, 5 = *xz* and 6 = *xy*), σ_v and η_u are the components of the stress and pure strain second-rank tensors. Second-order elastic moduli were calculated with the automated procedure implemented in the CRYSTAL code, and described in dedicated literature (Perger *et al.*, 2009). These routines were already recently applied for different minerals (Ulian & Valdrè, 2017, 2019), obtaining results in good agreement with the experimental ones. Single-crystal elastic properties, namely Young's modulus (E), linear compressibility (β), shear modulus (μ) and Poisson's ratio (υ) were calculated from the elastic moduli using the QUANTAS code (Ulian & Valdrè, 2022b), with well-known directional relations (see Gaillac *et al.*, 2016, Marmier *et al.*, 2010, Nye, 1957, Ulian *et al.*, 2018). Voigt and Reuss equations were employed to calculate the average elastic properties considering the system as a polycrystalline aggregate as explained by Nye (1957).

The program VESTA (Momma & Izumi, 2008) was used to create graphical representations of the mineral.

3. Results and Discussion

3.1. Structure at equilibrium and under hydrostatic compression

The isolated (ideal) cage As_4S_4 molecule belongs to the $\bar{4}2m$ point group (D_{2d} in Schoenflies notation) and is made of four arsenic atoms (1 irreducible) that form a disphenoid and four sulphurs (1 irreducible) forming a square that intersects the As polyhedron (see **Fig.1**). Within the molecule, each As is bonded to another arsenic and two sulphur atoms at 2.5642 Å and 2.2242 Å, respectively (see **Table 1**).

When the As_4S_4 molecule is inside the realgar crystal (Z = 4), it loses all its symmetry (point group 1, or C_1 in Schoenflies notation) and all the atoms are irreducible. However, due to the $P2_1/n$ space group symmetry, a single cage-like molecule of 8 atoms is sufficient to build the whole unit cell, which contains 32 atoms. The results of the optimization of the realgar unit cell at the DFT/PBEh-3c level performed in the present study are reported in **Table 1**. In general, our simulations at 0 K are in good agreement with the experimental synchrotron powder diffraction refinements at room temperature (see Hejny *et al.*, 2012), with variations of –0.1%, –2.0% and –2.3% for the *a*, *b* and *c* lattice parameters, respectively, and an increase of the β cell angle by ca. 0.5%, resulting in an overall underestimation of the unit cell volume of about 4.5%.

Table 1 Crystal structure (lattice parameters) and internal geometry (bond lengths and angles) of realgar as obtained from theoretical and experimental refinements. σ is the standard deviation of the related bond length or angle.

Parameter	α-As_4S_4		Experimental		Theoretical	
	Bulk[1]	*Cage*[1]	*Bulk*[2]	*Bulk*[3]	PW91[3]	PBE-D2[4]
s.g.	$P2_1/n$	D_{2d}	$P2_1/n$	$P2_1/n$	$P2_1/n$	$P2_1/n$
a (Å)	9.2467	-	9.328	9.253	9.242	9.403
b (Å)	13.3918	-	13.578	13.662	13.679	13.703
c (Å)	6.4508	-	6.952	6.603	6.662	6.586
β (°)	105.77	-	106.6	105.23	108.75	106.22
V (Å^3)	768.732	-	800.1	805.4	797.5	814.8
Bonds (Å)						
As1 – S1	2.2411	-	-	2.242	-	2.282
As1 – S2	2.2324	-	-	2.232	-	2.272
As2 – S1	2.2464	-	-	2.243	-	2.284
As2 – S3	2.2353	-	-	2.238	-	2.280
As3 – S2	2.2528	-	-	2.247	-	2.287
As3 – S4	2.2348	-	-	2.238	-	2.277
As4 – S3	2.2311	-	-	2.231	-	2.273
As4 – S4	2.2304	-	-	2.228	-	2.271
<As–S>	2.2380	2.2242	-	2.237	-	2.278
$\sigma_{As–S}$	0.0075	-	-	0.006	-	0.006
As1 – As4	2.5478	-	-	2.571	-	2.642
As2 – As3	2.5442	-	-	2.566	-	2.629
<As–As>	2.5460	2.5642	-	2.569	-	2.636
Angles (°)						
S1–S2–S4	89.65	-	-	-	-	-
S2–S4–S3	89.84	-	-	-	-	-
S4–S3–S1	90.35	-	-	-	-	-
S3–S1–S2	90.15	-	-	-	-	-
<S–S–S>	90.00	90.00	-	-	-	-
$\sigma_{S–S–S}$	0.27	-	-	-	-	-

1 – present work; 2 – Tuktabiev *et al.* (2009); 3 – Hejny *et al.* (2012); 4 – Caratelli *et al.* (2017).

The cohesive energy ΔE_{coh} was computed as:

$$\Delta E_{coh} = E_{mol} - E_{bulk}/Z \quad (4)$$

where E_{bulk} is the energy of the unit cell of the mineral, E_{mol} is the energy of the As_4S_4 molecule in the gas phase, and Z is the number of molecules in the unit cell. As expressed by the formula above, the cohesive energy is the energy required to separate the solid in its constituent cage-like molecules, hence it is a positive quantity. The calculated ΔE_{coh} value for realgar is 146.1 kJ mol^{-1}, which is in line with the interaction energy between As_4S_4 dimers (53.0 kJ mol^{-1}) computed at the Møller-Plesset level of theory reported in a previous study of Gibbs and collaborators (2011). The cohesive energy of realgar is also comparable with other molecular solids like urea (Civalleri *et al.*, 2008), albeit the molecules in this system are held together by a hydrogen bond network rather than van der Waals

interactions. This very high energy is due to the high polarizability of As and S atoms, which led to many intermolecular interactions between the cage-like molecules. Indeed, it was observed that there are 32 intermolecular interaction paths in the crystal structure from each As_4S_4 molecule towards 12 nearest-neighbour equivalent molecules, *i.e.*, 2 S---S, 7 As---As and 23 As---S (Gibbs *et al.*, 2011). It is worth noting that this energy value is already corrected for the BSSE by using the geometrical counterpoise approach (*vide supra*).

The cohesive energy ΔE_{coh} can also be divided into two contributions, the first one related to the conformational change of the molecule from the crystalline framework to the gas phase (ΔE_{conf}), and the second due to the sublimation energy (ΔE_{subl}):

$$\Delta E_{coh} = \Delta E_{conf} + \Delta E_{subl} \quad (5)$$

According to our simulations, the conformational energy is ΔE_{conf} = 1.6 kJ mol^{-1} and ΔE_{subl} = 144.5 kJ mol^{-1}, and as expected for a van der Waals structure, the ΔE_{conf} value is almost negligible. Noteworthy, to the authors' knowledge, this is the first time these energy terms are reported for realgar, which could be useful and exploited as a comparison basis for both experimentalists and theoreticians.

Table 2 reports the evolution of the lattice parameters and internal geometry (bond distances and angles, and distance between the centres of mass of the cage-like molecules) of α-As_4S_4 as a function of pressure. To calculate this data, we performed a volume-constrained optimization of the both the unit cell parameters and internal geometry, considering six volumes between 88% and 106% (step of 3%) of the unit cell relaxed at no applied pressure. Then, the pressure state at each compression state was calculated from the first derivative of the total energy *vs* volume curve, $E(V)$. An automated procedure implemented in the CRYSTAL code was employed (Erba *et al.*, 2014). A graphical representation of the variation of the unit cell volume and lattice vectors with pressure is shown in **Fig.2**, together with experimental ones from single-crystal XRD by Hejny *et al.* (2012) and theoretical data by Caratelli *et al.* (2017).

We considered both expansions and compressions of the unit cell to better describe the elastic behaviour of realgar, which is highly anisotropic, with larger variations observed for the *b* lattice parameter than for the *a* and *c* ones. The internal geometry of the molecules shows very low variation with pressure, with maximum absolute values of 1.0% and 0.5% for the As – As and As – S bond distances, respectively. By increasing pressure, all the bonds shrink but the As1 – S1 and the As3 – S2, which on the contrary stretch, in agreement with previous experimental and theoretical findings (Tuktabiev *et al.*, 2009; Hejny *et al.*, 2012; Caratelli *et al.*, 2017). Instead, the distance between the centres of mass of the As_4S_4 units shows variations up to about 9% in the explored pressure regime. These results show that the $V(P)$ behaviour is controlled by the variation of the void space between the As_4S_4 cage-like molecules, i.e., the packing density increases, which is consistent with a mineral

characterized by van der Waals interactions. This behaviour also justifies the higher compressibility of the **b**-axis, because along that direction the structure has the lowest packing, thus there is room to accommodate the cage-like molecules when the mineral is compressed. In addition, the evolution of the unit cell structure with pressure shows no abrupt changes up to 3.68 GPa, indicating the mineral is stable in these conditions.

Table 2 Crystal lattice and internal geometry (bond lengths, bond angles and distances between the centres of mass of the cage-like molecules) of realgar performed with DFT/PBEh-3c simulations. σ is the standard deviation of the related bond length or angle.

Parameter	**Pressure** (GPa)						
	–0.74	–0.35	–0.03	0.20	0.98	2.08	3.68
a (Å)	9.3263	9.2824	9.2467	9.2207	9.1443	9.0565	8.9463
b (Å)	13.8080	13.5414	13.3918	13.3008	13.0792	12.8723	12.6791
c (Å)	6.5723	6.4965	6.4508	6.4220	6.3494	6.2785	6.1997
β (°)	105.61	105.70	105.77	105.82	105.98	106.16	106.02
V (Å^3)	815.168	786.137	768.732	757.762	730.053	703.020	675.936
Bonds (Å)							
As1 – S1	2.2403	2.2408	2.2411	2.2412	2.2414	2.2414	2.2407
As1 – S2	2.2348	2.2335	2.2324	2.2317	2.2294	2.2264	2.2219
As2 – S1	2.2467	2.2466	2.2464	2.2461	2.2452	2.2438	2.2412
As2 – S3	2.2368	2.2360	2.2353	2.2348	2.2330	2.2306	2.2287
As3 – S2	2.2519	2.2526	2.2528	2.2529	2.2527	2.2520	2.2497
As3 – S4	2.2360	2.2354	2.2348	2.2343	2.2328	2.2305	2.2270
As4 – S3	2.2321	2.2316	2.2311	2.2306	2.2292	2.2271	2.2228
As4 – S4	2.2315	2.2309	2.2304	2.2300	2.2287	2.2271	2.2230
<As–S>	2.2388	2.2384	2.2380	2.2377	2.2366	2.2349	2.2319
$\sigma_{As–S}$	0.0067	0.0072	0.0075	0.0077	0.0083	0.0090	0.0099
As1 – As4	2.5549	2.5508	2.5478	2.5457	2.5395	2.5321	2.5198
As2 – As3	2.5514	2.5472	2.5442	2.5421	2.5358	2.5284	2.5217
<As–As>	2.5532	2.5490	2.5460	2.5439	2.5377	2.5303	2.5208
c1 --- c2	5.9251	5.8958	5.8750	5.8607	5.8205	5.7763	5.7149
c1 --- c3	7.5492	7.4745	7.4292	7.4004	7.3260	7.2515	7.1549
c1 --- c4	7.0494	6.9047	6.8233	6.7738	6.6534	6.5414	6.4386
c3 --- c4	13.3514	13.1273	12.9995	12.9210	12.7279	12.5452	12.3546
Angles (°)							
S1–S2–S4	89.79	89.71	89.65	89.63	89.56	89.44	89.39
S2–S4–S3	89.86	89.88	89.84	89.87	89.83	89.78	89.69
S4–S3–S1	90.18	90.27	90.35	90.38	90.49	90.66	90.78
S3–S1–S2	90.16	90.14	90.15	90.12	90.11	90.11	91.13
<S–S–S>	90.00	90.00	90.00	90.00	90.00	90.00	90.25
$\sigma_{S–S–S}$	0.18	0.22	0.27	0.28	0.35	0.45	0.73

The energy as a function of volume curve, $U(V)$, was fitted with the volume-integrated third-order Birch−Murnaghan (BM3) equation of state (Birch, 1947, Hebbache & Zemzemi, 2004):

$$U(V) = U_0 + \frac{9}{16} B_0 V_0 \left\{ B' \left[\left(\frac{V_0}{V} \right)^{-2/3} - 1 \right]^3 + \left[\left(\frac{V_0}{V} \right)^{-2/3} - 1 \right]^2 \left[6 - 4 \left(\frac{V_0}{V} \right)^{-2/3} \right] \right\} \quad (6)$$

with V_0 the zero-pressure volume, B_0 and B' the bulk modulus and its pressure derivative, respectively. The fitting procedure was performed using the QUANTAS code (Ulian & Valdrè, 2022b). The obtained parameters are V_0 = 767.13(9) Å^3, B_0 = 15.73(8) GPa and B' = 9.1(2).

These results are in line with the experimental determinations of Tuktabiev *et al.* (2009), whose Murnaghan equation of state results were B_0 = 8.1(5) GPa and B' = 9.0(5). Hejny *et al.* (2012) employed the third-order Birch-Murnaghan formulation to describe the single-crystal experimental data, obtaining V_0 = 799.4(2.4) Å^3, B_0 = 10.5(4) GPa and B' = 8.7 (fixed). This latter fixed value was obtained from fitting the $U(V)$ curve from DFT simulations, where the B_0 and B' parameters were calculated as 10.9(2) GPa and 8.7(2), respectively. As previously explained by Hejny *et al.* (2012), the slight difference between the two experimental results could be due to the different high-pressure experimental techniques and conditions, in particular the method to maintain the hydrostatic setup. Our results well correlate with both experimental findings, considering that our DFT simulations were carried out neglecting any thermal effect, even zero-point motion, while the high-pressure measurements on the realgar single-crystals were performed at room temperature (Tuktabiev *et al.*, 2009; Hejny *et al.*, 2012). However, the density functional simulation of Hejny and collaborators (2012) showed a softer behaviour of realgar than ours. We suggest that the absence of weak van der Waals interactions in the theoretical treatment of the mineral performed by Hejny *et al.* (2012) is the most probable source of this slight discrepancy. Still, other factors could contribute to the difference, *e.g.*, the use of different atomic basis sets and DFT functional (PW91). In fact, standard generalized gradient functionals such as PW91 typically result in softer elastic behaviour of crystalline solids. Caratelli and co-workers (2017) obtained from periodic PBE simulations corrected with the DFT-D2 scheme (Grimme, 2006) B_0 = 14.0 GPa and B' = 4.9, which are in good agreement with our data. The slightly stiffer behaviour with pressure, as highlighted by the smaller B' value, could be due to the different theoretical framework employed by Caratelli *et al.* (2012), *i.e.*, the basis sets (plane waves versus Gaussian-type orbitals) and the implementation of the long-range interactions (D2 versus D3 schemes). The latter is the most probable, because the D2 correction tends to overestimate the forces with respect to the D3 one.

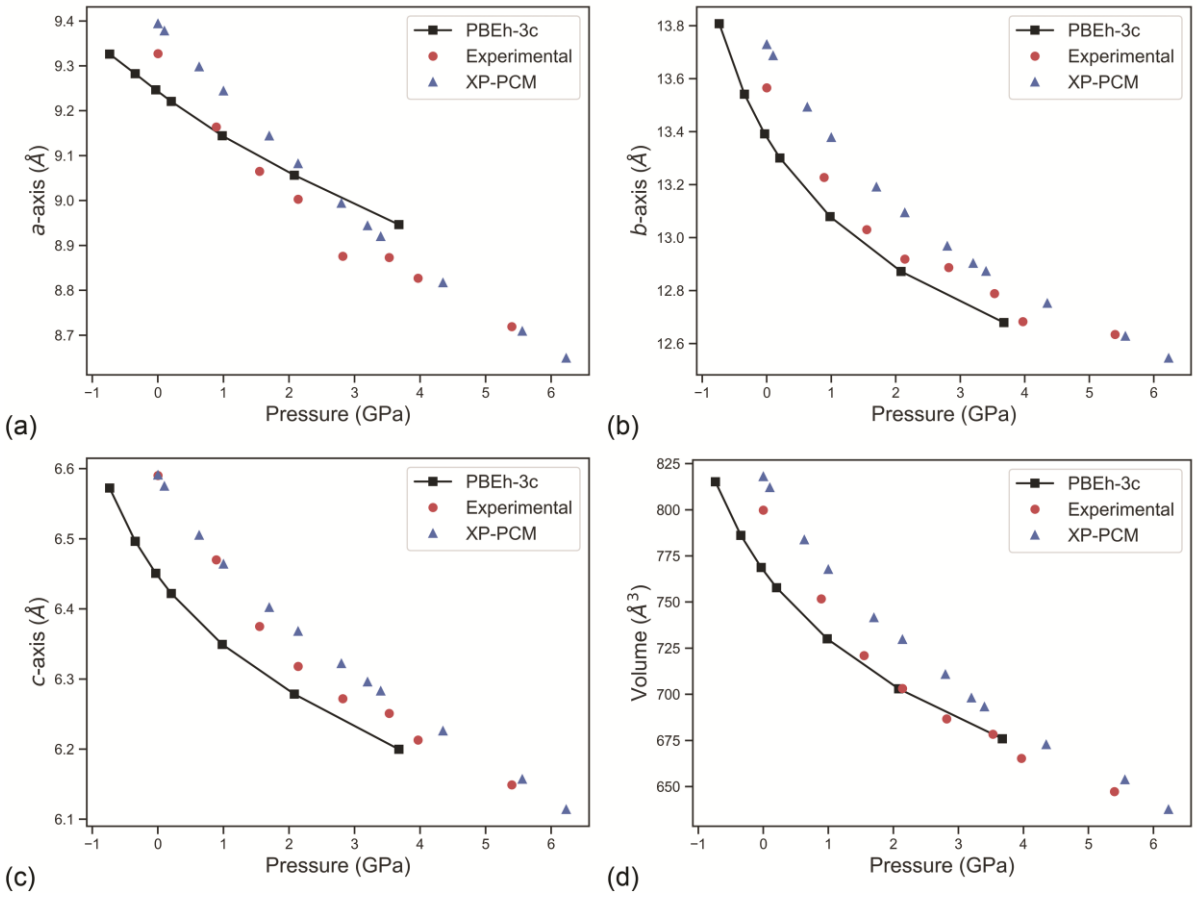

Figure 2 Evolution with the hydrostatic pressure of (a) **a-**, (b) **b-**, (c) **c**-axis lengths and (d) unit cell volume of realgar, as obtained from the present DFT/PBEh-3c simulations (black symbols and lines), compared to previous experimental results of Hejny *et al.* (2012) and the theoretical study of Caratelli *et al.* (2017) at the PBE-D2 level of theory.

3.2. Elastic moduli

To calculate the elastic moduli of realgar, the crystal system was oriented with the **b** and **c** lattice vectors parallel to the *x* and *z* Cartesian directions, respectively. The 6 × 6 Voigt's **C** matrix of the 13 independent elastic moduli for a monoclinic crystal presents then the following form:

$$\mathbf{C} = \begin{pmatrix} C_{11} & C_{12} & C_{13} & \cdot & C_{15} & \cdot \\ & C_{22} & C_{23} & \cdot & C_{25} & \cdot \\ & & C_{33} & \cdot & C_{35} & \cdot \\ & & & C_{44} & \cdot & C_{46} \\ & & & & C_{55} & \cdot \\ & & & & & C_{66} \end{pmatrix} \quad (7).$$

Our DFT/PBEh-3c simulations resulted in C_{11} = 29.78 GPa, C_{22} = 22.22 GPa, C_{33} = 32.88 GPa, C_{44} = 7.37 GPa, C_{55} = 7.23 GPa, C_{66} = 18.12 GPa, C_{12} = 14.34 GPa, C_{13} = 10.60 GPa, C_{23} = 7.87 GPa, C_{15} = –1.48 GPa, C_{25} = –0.04 GPa, C_{35} = –1.17 GPa, C_{46} = 0.05 GPa. The elastic properties, i.e., the bulk modulus B, the shear modulus μ, the Young's modulus E and the Poisson's ratio υ (see Nye, 1957), assuming the mineral as a polycrystalline sample are reported in **Table 3** as Voigt (upper bound), Reuss (lower bound) and Hill (average) values (Ulian & Valdrè, 2019).

The bulk modulus values obtained from the equation of state fitting (B_0 = 15.73) and the elastic moduli (Reuss bound, 16.1 GPa) are very similar, meaning that the present DFT simulations are consistent. The difference of about 1–3% between the elastic data related to the upper and lower bounds highlights the slight anisotropic behaviour of the mineral, in agreement with the hydrostatic compression results (see **Fig.2**).

Directional variations of the elastic properties of realgar are graphically reported in **Fig.3**, whose analysis clearly shows the anisotropic behaviour of the mineral, in agreement with the previously reported equation of state results.

To our knowledge, experimental and theoretical data of the elastic moduli and their derived properties of realgar are not available in the scientific literature. We highlight that the employed athermal conditions, *i.e.*, thermal effects are neglected, and the presence of Pulay forces, a well-known small deviation effect occurring in the analysis of the stress tensor in self-consistent field calculations with Gaussian-type orbitals basis sets (see Francis & Payne, 1990, Ulian & Valdrè, 2022a) typically result in slightly higher elastic moduli than room temperature ones.

Table 3 Elastic properties of realgar α-As_4S_4 according to the Voigt, Reuss and Hill averaging schemes for polycrystalline materials.

	B **(GPa)**	***E*** **(GPa)**	***μ*** **(GPa)**	***υ***
Voigt	16.7	25.0	10.0	0.250
Reuss	16.1	21.4	8.4	0.279
Hill	16.4	23.2	9.2	0.264

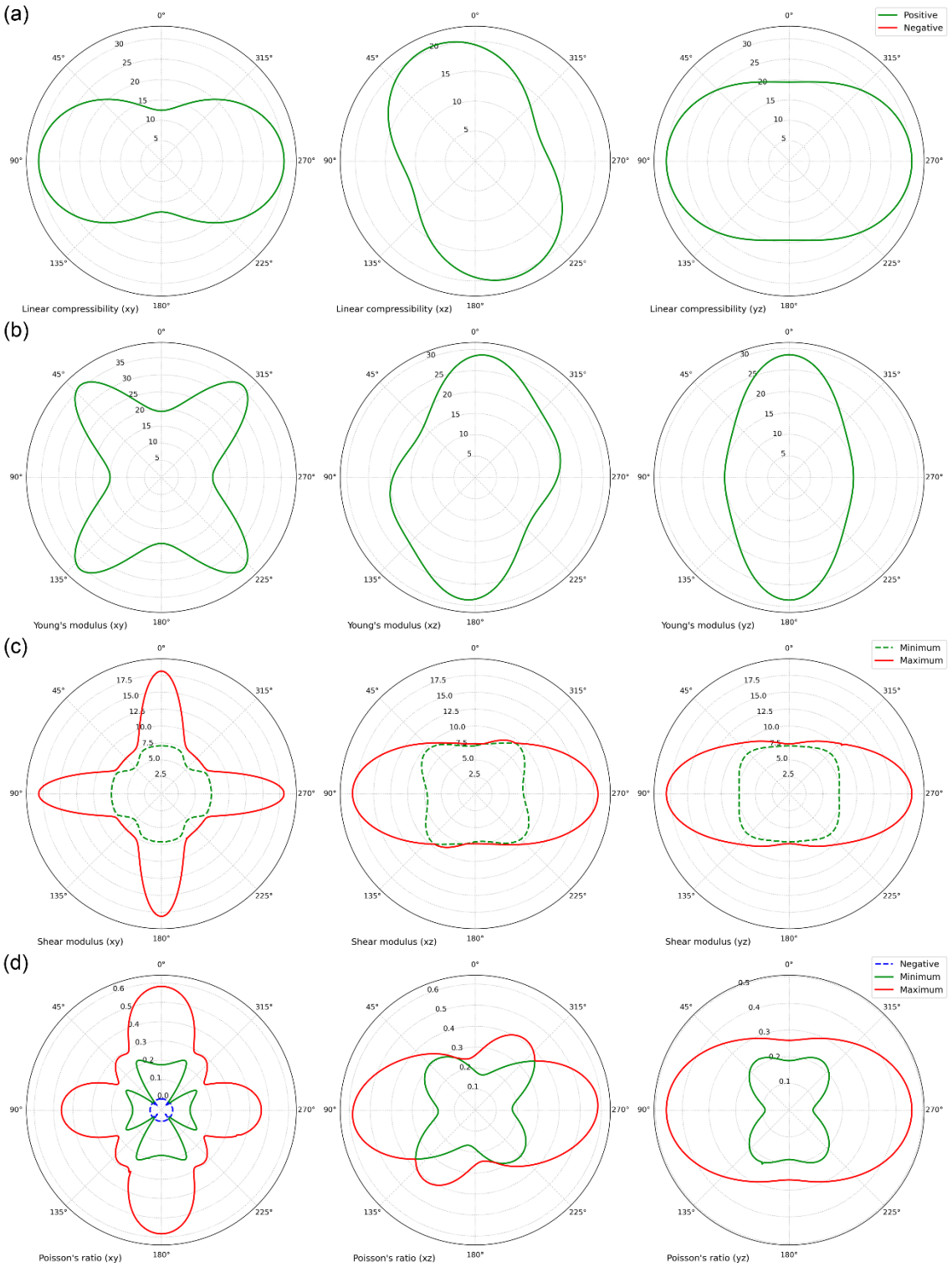

Figure 3 Directional variations of: (a) linear compressibility $\beta = 1/B$; (b) Young's modulus E; (c) shear modulus μ; (d) Poisson's ratio υ of realgar, reported on xy, xz and yz planes.

3.3. Infrared and Raman frequencies

The isolated As_4S_4 cage-like molecule possesses $8 \times 3 = 24$ degrees of freedom associated with the atomic displacements in the three-dimensional space. The vibrational normal modes can be obtained from the reduction of the total representation Γ_{mol} into irreducible representations (IRREPs) according to the D_{2d} symmetry group:

$$\Gamma_{mol} = 3A_1 \oplus 3A_2 \oplus 2B_1 \oplus 4B_2 \oplus 6E,$$

with E modes being doubly degenerate. In Γ_{mol} there are three rigid translations ($B_2 \oplus E$) and three rotations ($A_2 \oplus E$) of the whole molecule, and the remaining 18 IRREPs are related to the internal (or intramolecular) modes. Furthermore, it is worth remembering that B_2 and E modes are active in both infrared and Raman spectroscopies, whereas A_1 and B_1 are active only in Raman, and A_2 modes are silent.

As previously mentioned, the realgar cage-like molecule in the monoclinic crystal structure lowers its point symmetry to C_1 and, as a result, all the vibrational modes v, which in solids are called phonons or optical modes, become spectroscopically active. In addition, it is expected that the 18 normal vibrations split into four components, two active in Raman and two active in IR. These numbers are doubled when considering the modes with E symmetry (eight modes, 4 in Raman and 4 in IR). Then, for α-As_4S_4 (space group $P2_1/n$), the classification of the $32 \times 3 = 96$ degrees of freedom of the total representation of the solid Γ_{solid} is the following:

$$\Gamma_{solid} = 24A_g \oplus 24A_u \oplus 24B_g \oplus 24B_u,$$

where the subscripts “g” and “u” indicate the mode being symmetric and antisymmetric to the inversion symmetry operation, respectively. Also, the A_g and B_g modes are active in Raman, whereas the A_u and B_u are infrared modes because of the mutual exclusion principle. In the solid, $A_u \oplus 2B_u$ are acoustic ones that have zero frequency in the central zone of the Brillouin zone ($\mathbf{q} = 0$), thus there are 93 nondegenerate phonons. An illustrative representation of the relationship between the vibrational modes in the As4S4 molecule and the Γ-point phonon spectrum of realgar crystal is shown in the work of Zallen and Slade (1978).

The results of our simulations performed with the PBEh-3c of the vibrational properties of both the isolated realgar-like molecule and the α-As_4S_4 mineral phase are reported in **Table 4**, alongside previous experimental and theoretical investigations for a comparison (Caratelli *et al.*, 2017, Muniz-Miranda *et al.*, 1996). Each mode was assigned to specific intramolecular atomic motions using the analysis of potential energy distribution (PED) provided by the CRYSTAL code, labelling bending and stretching modes as δ and σ, respectively.

Table 4 Vibrational frequencies v of isolated As_4S_4 cage-like molecule and realgar α-As_4S_4 calculated at the DFT/PBEh-3c level of theory, subdivided in the different irreducible representations (IRREP) and compared to the available experimental and theoretical data.

Molecular As_4S_4[1]			**IR α-As_4S_4[1]**		**Raman α-As_4S_4[1]**		**Exp.[2]**	**PBE-D2[3]**
IRREP	*v* (cm^{-1})	*Assignment*	*IRREP*	*v* (cm^{-1})	*IRREP*	*v* (cm^{-1})		
A_2	105.7	$\delta_{S–As–S}$	A_u	124.1	B_g	129.3	–	
			B_u	124.3	A_g	130.2		
B_1	150.7	$\delta_{S–As–S} + \delta_{As–S–As}$	A_u	155.5	B_g	151.1	144	144
			B_u	155.9	A_g	151.4		
E	165.7	$\delta_{S–As–S}$	A_u	175.1	B_g	171.8	167	170
			B_u	176.4	A_g	172.2		
			B_u	177.3	B_g	177.4		
			A_u	179.3	A_g	179.6		
B_2	190.4	$\sigma_{As–As}$	B_u	192.9	A_g	190.0	173	184
			A_u	197.1	B_g	191.0		
A_1	191.7	$\delta_{S–As–S}$	B_u	207.4	B_g	206.4	184	193
			A_u	208.1	A_g	207.4		
E	222.3	$\delta_{S–As–S} + \delta_{As–S–As}$	B_u	212.5	A_g	217.3	210	224
			B_u	217.0	A_g	219.6		
			A_u	219.0	B_g	221.8		
			A_u	220.0	B_g	223.0		
A_1	229.5	$\delta_{S–As–S}$	B_u	231.4	A_g	235.4	196	213
			A_u	232.7	B_g	236.0		
B_2	228.3	$\delta_{As–S–As}$	B_u	236.3	A_g	232.8	222	229
			A_u	237.5	B_g	235.1		
A_2	329.8	$\sigma_{As–S}$	A_u	331.5	B_g	332.1	330	325
			B_u	332.7	A_g	332.3		
E	355.4	$\sigma_{As–S}$	A_u	344.6	A_g	345.5	341	343
			B_u	347.9	B_g	349.1		
			A_u	348.5	A_g	350.1		
			B_u	352.6	B_g	350.4		
B_1	363.0	$\sigma_{As–S}$	B_u	354.4	A_g	354.9	345	353
			A_u	355.6	B_g	356.4		
A_1	378.9	$\sigma_{As–S}$	B_u	367.8	A_g	365.7	355	378
			A_u	371.0	B_g	367.0		
B_2	382.2	$\sigma_{As–S}$	A_u	372.2	B_g	370.7	376	365
			B_u	373.4	A_g	373.4		
E	383.3	$\sigma_{As–S}$	B_u	374.1	A_g	374.6	370	385
			A_u	375.0	B_g	376.4		
			A_u	380.2	A_g	381.0		
			B_u	380.8	B_g	384.5		

1 – present work; 2 – Raman data of Muniz-Miranda *et al.* (1996); 3 – DFT/PBE-D2 results of Caratelli *et al.* (2017)

Lattice phonons, i.e., vibrational motions associated with rigid translations and rotations of the cage-like molecules are not reported in **Table 4** for the sake of clarity, but will be discussed in detail when presenting the pressure-dependency of the IR/Raman modes (*vide infra*). The here reported

assignment is consistent to that provided by Muniz-Miranda *et al.* (1996), which resulted from the analysis of the IR/Raman spectra of the mineral obtained from both spectroscopic measurements and the calculation of the vibrational frequencies with a simplified force field approximation. As expected, the calculated modes of realgar are generally overestimated, i.e., they have a higher frequency than the experimental ones because of both the harmonic approximation framework used to calculate them and the athermal (0 K) conditions. However, the results are in line and comparable to those reported in the literature. As expected, compared to the periodic calculations performed with the PBE-D2 approach (Caratelli *et al.*, 2017), our normal modes are slightly overestimated because it is known that the hybrid functionals (e.g., PBEh) predict larger vibrational frequencies values compared to standard generalized gradient approximation functionals, such as PBE (Pascale *et al.*, 2004b). In addition, a small contribution could also be due to the use of the DFT-D3 scheme that generally increases the intermolecular interactions more than the DFT-D2 approach (Ulian *et al.*, 2021).

The blue- and red-shifts of the vibrational modes as a function of the pressure can also be described using different equations that correlate the vibrational frequency v to the unit cell volume V. In the present work, we employed the so-called mode-Grüneisen (or mode-γ) parameters, γ_p, which are commonly used in mineralogy and geophysics (Anderson, 1995). The mode-γ parameters were obtained for each p^{th} mode as:

$$\gamma_p = -\frac{\partial \ln \nu_p}{\partial \ln V} = -\frac{V}{\nu_p}\frac{\partial \nu_p}{\partial V} \quad (8).$$

For each normal mode, γ_p was computed through the analytic first derivative at each volume (pressure) of the second-order polynomial, resulting from the fitting of the numerical $\nu_p(V)$ curves, as recently reported for aragonite (Ulian & Valdrè, 2023). The resulting mode-Grüneisen parameters γ_p are presented in **Table 5**, and their distribution with frequency is graphically shown in **Fig.4**. It can be noted that all the γ_p values are positive, meaning that the phonon frequencies increase with pressure, and hence reduce with volume. It is worth noting that lattice phonons showed the highest blue shifts ($\gamma_p >> 1$), which can be explained by the increased interaction between the As_4S_4 molecules that are brought closer to each other during compression. Conversely, the intramolecular vibrations are less affected by pressure, with mode-Grüneisen parameters lower than 0.8, which is in line with the structural observations.

Our simulations are generally in good agreement with previous experimental measurements, where various authors reported the pressure variation of the Raman modes of realgar (see for instance Zallen & Slade, 1978, Hejny *et al.*, 2012).

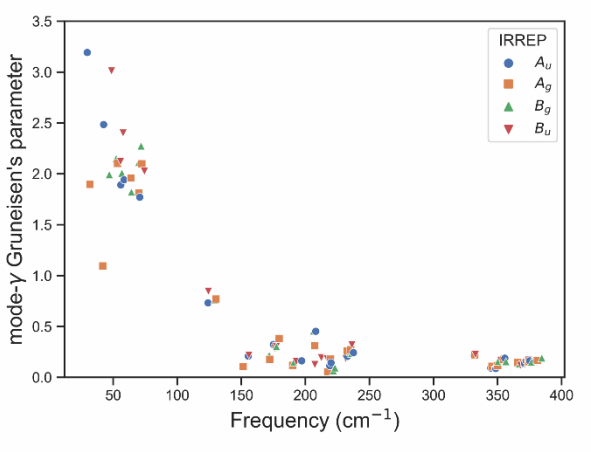

Figure 4 Mode-γ parameters as a function of frequency obtained from DFT/PBEh-3c simulations, subdivided into the different irreducible representations (IRREPs).

Table 5 Present calculated γ_p values for the phonon modes active in infrared ($A_u + B_u$) and Raman ($A_g + B_g$).

A_u			B_u			A_g			B_g		
ν (cm^{-1})	γ_p	†	ν (cm^{-1})	γ_p	†	ν (cm^{-1})	γ_p	†	ν (cm^{-1})	γ_p	†
0.0	-	-	0.0	-	-	31.9	1.90	2.68	47.0	1.99	1.57
29.8	3.19	2.81	0.0	-	-	41.9	1.10	1.78	52.4	2.15	1.91
42.6	2.48	2.24	48.7	3.01	1.99	53.5	2.10	1.84	56.8	2.01	1.87
56.0	1.89	1.40	55.8	2.12	1.70	63.9	1.96	2.03	64.2	1.82	1.70
58.5	1.94	1.99	57.8	2.40	2.50	70.1	1.81	1.96	70.0	2.11	2.07
70.8	1.77	1.79	74.4	2.03	1.86	72.4	2.10	2.17	71.8	2.27	2.24
124.1	0.73	0.54	124.3	0.85	0.66	130.2	0.77	0.44	129.3	0.76	0.41
155.5	0.21	0.18	155.9	0.22	0.21	151.4	0.11	0.17	151.1	0.11	0.16
175.1	0.32	0.16	176.4	0.28	0.07	172.2	0.18	0.00	171.8	0.22	0.17
179.3	0.39	0.32	177.3	0.30	0.18	179.6	0.38	0.17	177.4	0.30	0.15
197.1	0.16	0.07	192.9	0.16	0.07	190.0	0.12	0.03	191.0	0.15	0.13
208.1	0.45	0.38	207.4	0.13	-0.01	207.4	0.31	0.34	206.4	0.46	0.35
219.0	0.11	0.08	212.5	0.19	0.19	217.3	0.05	0.04	221.8	0.06	0.03
220.0	0.14	0.11	217.0	0.18	0.21	219.6	0.18	0.00	223.0	0.09	0.12
232.7	0.21	0.13	231.4	0.18	0.04	232.8	0.26	0.26	235.1	0.25	0.20
237.5	0.24	0.16	236.3	0.32	0.17	235.4	0.27	0.22	236.0	0.24	0.20
331.5	0.21	-0.02	332.7	0.23	-0.04	332.3	0.22	0.04	332.1	0.22	0.03
344.6	0.09	-0.10	347.9	0.07	-0.04	345.5	0.11	-0.09	349.1	0.14	-0.04
348.5	0.09	0.11	352.6	0.17	0.07	350.1	0.12	0.11	350.4	0.16	0.06
355.6	0.19	0.04	354.4	0.18	0.12	354.9	0.17	0.05	356.4	0.15	0.06
371.0	0.14	0.04	367.8	0.12	0.02	365.7	0.15	0.04	367.0	0.13	0.09
372.2	0.16	0.06	373.4	0.14	0.05	373.4	0.15	-0.02	370.7	0.14	0.01
375.0	0.16	0.07	374.1	0.17	0.02	374.6	0.15	0.06	376.4	0.15	0.05
380.2	0.16	0.06	380.8	0.17	0.06	381.0	0.17	0.06	384.5	0.19	0.07

† mode-γ Grüneisen parameters calculated from the theoretical data of Caratelli and collaborators (2017).

We compared our simulations with other theoretical analysis and specifically related the present results obtained at the PBEh-3c level with those with the PBE-D2 level by Caratelli and collaborators (2017). The agreement between the two approaches is satisfactory, with a general underestimation provided by the standard generalized gradient approximation functional PBE, as can be noted from **Fig.5**. Some other computational parameters used by the cited authors, *e.g.*, the plane wave basis sets, the smaller size of the *k* point grid (10 *k* points), could also explain the small differences between the results. Most of the γ_p values reported by Caratelli *et al.* (2017), recalculated using Grüneisen's formulation for a direct comparison (see **Table 5**), are positive, with just a few red-shifted phonons that showed an almost constant frequency value up to about 6 GPa ($|\gamma_p| < 0.1$). Both our mode-Grüneisen parameters and the previous ones of Caratelli *et al.* (2017) are slightly underestimated with respect to experimental data (see Zallen & Slade, 1978, Hejny *et al.*, 2012) because of the absence of thermal effects. Moreover, as also suggested by Caratelli *et al.* (2017), the γ_p values from the experiments were calculated using two to three frequency values for each phonon modes, which could affect the accuracy of the results.

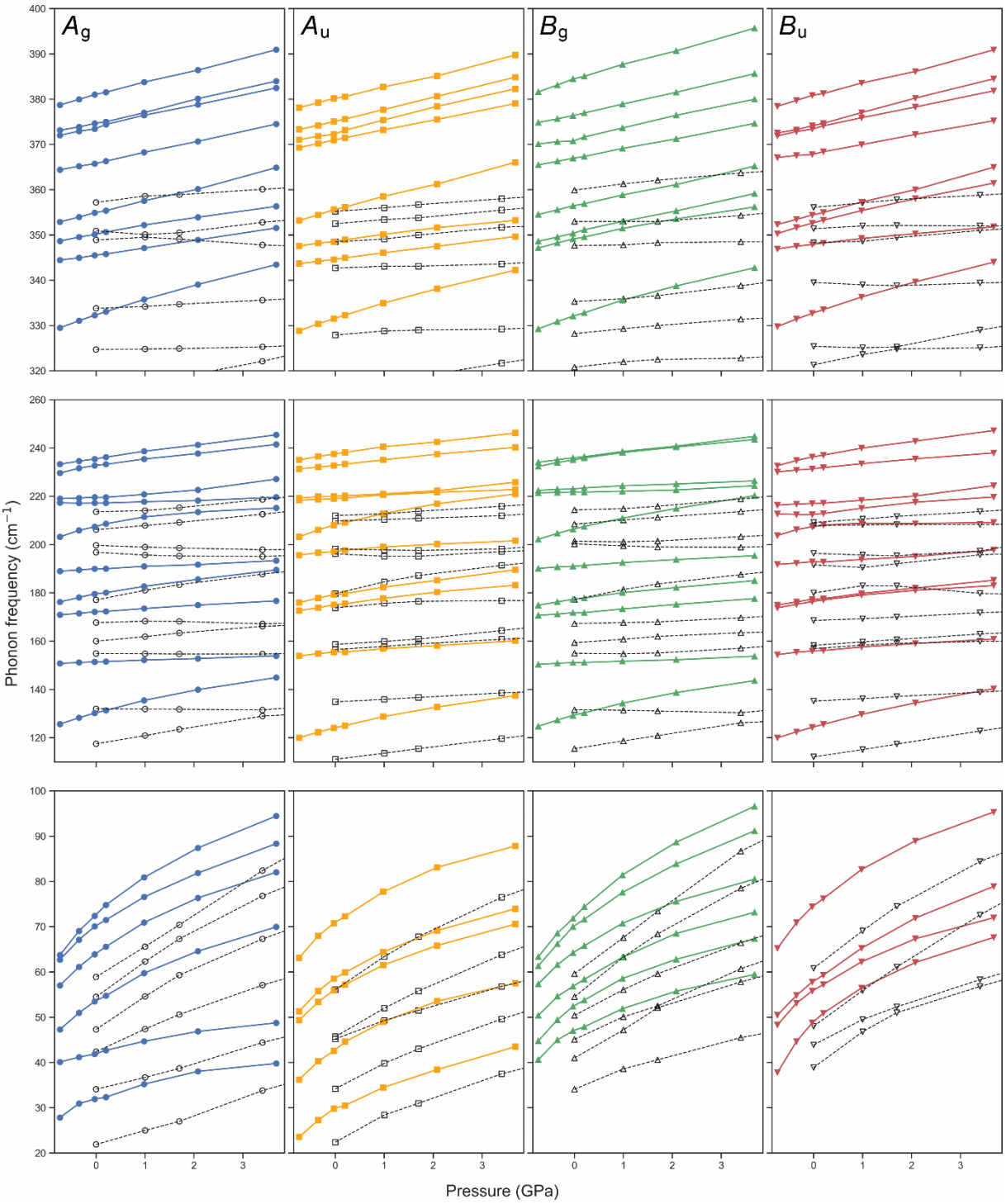

Figure 5 Evolution of the phonon frequencies with pressure in different regions of the IR and Raman spectra. Solid symbols are related to DFT/PBEh-3c results, whereas empty ones are associated with the PBE-D2 data of Caratelli *et al.* (2017). The lines are just simple guides for the eye.

3.4. Band structure and density of states

Because of the interest in possible optoelectronic applications, it is also important to address the electronic properties of α-As_4S_4. For this reason, we calculated the band structure of the mineral along the Γ – Z – D – B – Γ – A – E – Z – C_2 – Y_2 – Γ path in the reciprocal space and the atom-projected density of states (DOS). Both properties were simulated at equilibrium volume and under compression/expansion.

Fig.6a shows the band structure and the DOS of realgar between –10 eV and +10 eV when no pressure is applied. It can be noted that the valence (occupied) and conduction (unoccupied) bands are divided into groups and they are almost flat. The band gap is indirect and involves the topmost valence band near the Γ reciprocal point and the bottom of the conduction band in the A point, with *E*g = 3.99 eV. By varying pressure, the nature of the electronic transition does not change and there is an inverse relationship between the band gap energy and pressure (see **Fig.6b**). Compared to the experimental analysis of the optical absorption edge performed by Hejny *et al.* (2012), the present theoretical results are slightly overestimated, as well as to those obtained by the same authors using DFT/PBE simulations. A second deviation from the results reported by Hejny *et al.* (2012) is the nature of the band gap, which the cited authors reported as being direct.

In fact, standard generalized gradient approximation simulations typically underestimate the band gap E_g, as can be noted from the comparison in **Fig.6b**. Hybrid functionals are known to provide a better description of the electronic properties due to the contribution of a fraction of exact Hartree-Fock exchange, which generally increases the E_g values. In this specific case, the inclusion of 42% HF in the proposed theoretical approach is probably quite high, explaining the observed overestimation. Nevertheless, the trend of the band gap with pressure is correctly evaluated at the PBEh-3c level of theory.

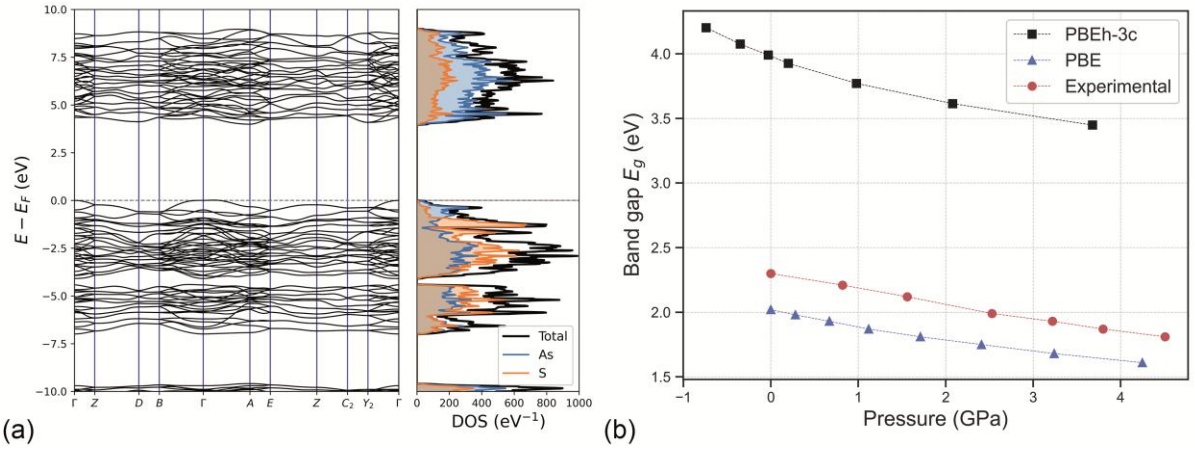

Figure 6 (a) Electronic band structure and atom-projected density of states of α-As4S4 in the energy range ± 10 eV. (b) Evolution of the band gap with pressure. Experimental (red circles) and theoretical

data at the DFT/PBE level of theory (blue triangles) of Hejny and collaborators (2012) are shown for comparison.

4. Conclusions

In the present work, we performed a density functional theory simulation to investigate the structural, elastic and vibrational properties of realgar α-As_4S_4, an important mineral for both fundamental minero-geological research and modern technological applications. Indeed, realgar is characterized by a distinct molecular nature, with strong covalent bonds within the As_4S_4 units that are held together by three-dimensional van der Waals interactions, similar to that of other inorganic and organic phases, such as sulphur S_8 and urea CH_4N_2O crystals, respectively. This peculiar feature explains the high compressibility of the mineral, as evinced from the equation of state results that adequately reproduced the experimental findings. At the atomic level, the As_4S_4 molecular units are almost unaffected by pressure, whereas the intermolecular volume strongly varies to accommodate the structural changes during compression/expansion. This also explains the higher shrink of the **b** lattice vector than the **a** and **c** ones during compression. We reported for the first time the cohesive energy ΔE_{coh} between the cage-like molecules within the crystal and further details on the mechanical properties of realgar by calculating the elastic moduli tensor. Albeit no theoretical data is available for a direct comparison of ΔE_{coh}, the results are consistent with those from crystalline structures characterized by long-range interactions between molecules (e.g., urea) and set a comparison basis for further experimental and theoretical studies. The infrared and Raman vibrational modes in equilibrium during hydrostatic compression are in line with previous experimental and theoretical studies, showing the blue-shift of the modes, with a higher variation for the lattice modes than for the intramolecular ones.

Realgar was also an interesting minero-structural test case to benchmark the PBEh-3c approach, which combines a global hybrid functional PBEh (with a high contribution from exact Hartree-Fock exchange) with both the DFT-D3 correction for treating long-range interactions and the geometrical counterpoise correction to remove the basis set superposition error. Indeed, this method was tested for well-known datasets of simple structures typically employed in quantum chemistry (e.g., the molecules and solids contained in the SS20 and POB tests) with good results, but its quality was never assessed for more complex structures such as α-As_4S_4. The present study showed that PBEh-3c is promising for quantum mineralogy applications, paving the road to its use for minerals such as graphite, sulphur and other weakly bound systems like phyllosilicates, however, careful analysis of the results and proper calibration is always suggested.

Acknowledgements The authors wish to thank the University of Bologna for supporting the present research.

References

Anderson, O. L. (1995). *Equation of state of solids for geophysics and ceramic science*. New York, US: Oxford University Press.

Avlonitou, L. (2016). *Journal of Archaeological Science: Reports* **7**, 668-678.

Becke, A. D. & Johnson, E. R. (2005). *Journal of Chemical Physics* **123**, 154101.

Bindi, L., Pratesi, G., Muniz-Miranda, M., Zoppi, M., Chelazzi, L., Lepore, G. O. & Menchetti, S. (2015). *Mineralogical Magazine* **79**, 121-131.

Birch, F. (1947). *Physical Review* **71**, 809-824.

Bonazzi, P. & Bindi, L. (2008). *Zeitschrift fur Kristallographie* **223**, 132-147.

Caratelli, C., Cammi, R., Chelli, R., Pagliai, M., Cardini, G. & Schettino, V. (2017). *Journal of Physical Chemistry A* **121**, 8825-8834.

Civalleri, B., Zicovich-Wilson, C. M., Valenzano, L. & Ugliengo, P. (2008). *CrystEngComm* **10**, 405-410.

Cutini, M., Maschio, L. & Ugliengo, P. (2020). *Journal of chemical theory and computation* **16**, 5244-5252.

Daniels, V. & Leach, B. (2004). *Studies in Conservation* **49**, 73-84.

Dovesi, R., Erba, A., Orlando, R., Zicovich-Wilson, C. M., Civalleri, B., Maschio, L., Rerat, M., Casassa, S., Baima, J., Salustro, S. & Kirtman, B. (2018). *Wiley Interdisciplinary Reviews-Computational Molecular Science* **8**, E1360.

Erba, A., Mahmoud, A., Belmonte, D. & Dovesi, R. (2014). *Journal of Chemical Physics* **140**, 124703.

Ernst, R. R. (2010). *Journal of Raman Spectroscopy* **41**, 275-284.

Francis, G. P. & Payne, M. C. (1990). *Journal of Physics-Condensed Matter* **2**, 4395-4404.

Gaillac, R., Pullumbi, P. & Coudert, F. X. (2016). *Journal of Physics-Condensed Matter* **28**, 275201.

Gibbs, G. V., Crawford, T. D., Wallace, A. F., Cox, D. F., Parrish, R. M., Hohenstein, E. G., Sherril, C. D. (2011). *Journal of Physical Chemistry A* **17**, 12933-12940.

Grimme, S. (2006). *Journal of Computational Chemistry* **27**, 1787-1799.

Grimme, S., Antony, J., Ehrlich, S. & Krieg, H. (2010). *Journal of Chemical Physics* **132**, 154104.

Grimme, S., Brandenburg, J. G., Bannwarth, C. & Hansen, A. (2015). *Journal of Chemical Physics* **143**, 054107.

Grimme, S., Ehrlich, S. & Goerigk, L. (2011). *Journal of Computational Chemistry* **32**, 1456-1465.

Hebbache, M. & Zemzemi, M. (2004). *Physical Review B* **70**, 224107.

Hejny, C., Sagl, R., Többens, D. M., Miletich, R., Wildner, M., Nasdala, L., Ullrich, A. & Balic-Zunic, T. (2012). *Physics and Chemistry of Minerals* **39**, 399-412.

Kruse, H. & Grimme, S. (2012). *Journal of Chemical Physics* **136**, 154101.

Li, T., Xie, Y. F., Yang, Y. M., Wang, C. S., Fang, X. Y., Shi, J. L. & He, Q. J. (2009). *Journal of Raman Spectroscopy* **40**, 1911-1918.

Marmier, A., Lethbridge, Z. A. D., Walton, R. I., Smith, C. W., Parker, S. C. & Evans, K. E. (2010). *Computer Physics Communications* **181**, 2102-2115.

Momma, K. & Izumi, F. (2008). *J. Appl. Crystallogr.* **41**, 653-658.

Monkhorst, H. J. & Pack, J. D. (1976). *Physical Review B* **8**, 5188-5192.

Muniz-Miranda, M., Sbrana, G., Bonazzi, P., Menchetti, S. & Pratesi, G. (1996). *Spectrochimica Acta - Part A Molecular Spectroscopy* **52**, 1391-1401.

Nye, J. F. (1957). *Physical properties of crystals*. Oxford: Oxford University Press.

Pascale, F., Zicovich-Wilson, C. M., Gejo, F. L., Civalleri, B., Orlando, R. & Dovesi, R. (2004a). *Journal of Computational Chemistry* **25**, 888-897.

Pascale, F., Tosoni, S., Zicovich-Wilson, C., Ugliengo, P., Orlando, R. & Dovesi, R. (2004b). *Chemical Physics Letters* **396**, 308-315.

Perdew, J. P., Burke, K. & Ernzerhof, M. (1996). *Physical Review Letters* **77**, 3865-3868.

Perger, W. F., Criswell, J., Civalleri, B. & Dovesi, R. (2009). *Computer Physics Communications* **180**, 1753-1759.

Prencipe, M., Pascale, F., Zicovich-Wilson, C. M., Saunders, V. R., Orlando, R. & Dovesi, R. (2004). *Physics and Chemistry of Minerals* **31**, 559-564.

Tkatchenko, A., Distasio, R. A., Car, R. & Scheffler, M. (2012). *Physical Review Letters* **108**, 236402.

Tuktabiev, M. A., Popova, S. V., Brazhkin, V. V., Lyapin, A. G. & Katayama, Y. (2009). *Journal of Physics Condensed Matter* **21**, 385401.

Tunega, D., Bucko, T. & Zaoui, A. (2012). *Journal of Chemical Physics* **137**, 114105.

Ulian, G., Moro, D. & Valdrè, G. (2018). *Composite Structures* **202**, 551-558.

Ulian, G., Moro, D. & Valdrè, G. (2021). *Physical Chemistry Chemical Physics* **23**, 18899-18907.

Ulian, G. & Valdrè, G. (2015). *American Mineralogist* **100**, 935-944.

Ulian, G. & Valdrè, G. (2017). *American Mineralogist* **102**, 347-356.

Ulian, G. & Valdrè, G. (2018). *International Journal of Quantum Chemistry* **118**, e25553.

Ulian, G. & Valdrè, G. (2019). *Physics and Chemistry of Minerals* **46**, 101-117.

Ulian, G. & Valdrè, G. (2022a). *Computational Materials Science* **212**, 111600.

Ulian, G. & Valdrè, G. (2022b). *Journal of Applied Crystallography* **55**, 386-396.

Ulian, G. & Valdrè, G. (2023). *Scientific Reports* **13**, 2725.

van Loon, A., Noble, P., Krekeler, A., Snickt, G., Janssens, K., Abe, Y., Nakai, I. & Dik, J. (2017). *Heritage Science* **5**, 26.

Yang, L., Dai, L., Li, H., Hu, H., Hong, M., Zhang, X. & Liu, P. (2021). *Geoscience Frontiers* **12**, 1031-1037.

Zallen, R. & Slade, M. L. (1978). *Physical Review B* **18**, 5775-5798.